



ELSEVIER

Contents lists available at ScienceDirect

Fire Safety Journal

journal homepage: www.elsevier.com/locate/firesaf

Radiative emissions measurements from a buoyant, turbulent line flame under oxidizer-dilution quenching conditions

J.P. White^a, E.D. Link^a, A.C. Trouvé^a, P.B. Sunderland^a, A.W. Marshall^{a,*}, J.A. Sheffel^b, M.L. Corn^b, M.B. Colket^b, M. Chaos^c, H.-Z. Yu^c

^a Department of Fire Protection Engineering, University of Maryland, College Park, MD 20742, USA

^b United Technologies Research Center, East Hartford, CT 06108, USA

^c FM Global Research Division, Norwood, MA 02062, USA

ARTICLE INFO

Article history:

Received 7 November 2014

Received in revised form

20 May 2015

Accepted 31 May 2015

Keywords:

Fire

Suppression

Extinction

Flame height

Loss fraction

Luminosity

Slot burner

ABSTRACT

This work features the suppression of buoyant, turbulent, methane- and propane-fueled diffusion flames. Flames are stabilized above a $5 \times 50 \text{ cm}^2$ slot burner surrounded by a co-flowing oxidizer. Nitrogen gas is added to the oxidizer to achieve suppression. Mean flame height, measured using a digital camera, increases with reducing oxidizer oxygen mole fraction (X_{O_2}), in agreement with scaling predictions. Visible emissions, measured using a photodiode, are found to decrease by six orders of magnitude with reducing X_{O_2} . This decrease is attributed to diminishing soot radiation, where sharp curves in the trends for both fuels coincide with changes in flame color from yellow to blue. Methane, but not propane, flames are found to experience a period of soot-free (blue) combustion prior to extinction. Infrared emissions are measured using a heat flux transducer and are interpreted using an infrared camera and multipoint radiation source model. Radiative loss fraction is found to decrease linearly with reducing X_{O_2} , where the slope of decline is affected by fuel sooting propensity. Flame extinction occurs as liftoff at $X_{O_2}=0.151$ for methane and $X_{O_2}=0.138$ for propane. An oxygen anchor, explored to resist liftoff, extended the flammable domain to $X_{O_2}=0.130$ for both fuels.

© 2015 Elsevier Ltd. All rights reserved.

1. Introduction

Fire suppression systems are ubiquitous as a means of promoting life safety and property protection from accidental fires. Despite their prevalence and the generally regarded reliability of such systems, there remains a limited understanding of the complex physical processes underlying suppression phenomena. An improved understanding of these phenomena is paramount to design innovation and advancement of fire suppression technologies.

A number of previous studies, both experimental and numerical, have explored the extinction behavior of flames. These studies have identified several important mechanisms for gas-phase suppression, including heat extraction, oxidizer/fuel dilution, aerodynamic disruption, and chemical inhibition [1–5]. Such studies have explored the weakening and extinction response of flames to suppression mechanisms, while also comparing the prevalence and relative efficacy of their effects [6–14]. Recent works have investigated large-scale fires in realistic

configurations, primarily to evaluate suppression performance in specific scenarios, while also delivering much needed data for the validation of suppression models [15–17]. Others have focused on developing scaling relationships to compare results from different sized configurations [18,19]. It is worth noting that most previous studies have featured small laminar flames, which have proven quite useful for exploring extinction theory [20–27] as well as establishing extinction-limit criteria for flames under quenching action [28–35].

What remains to be explored is how the noted suppression mechanisms dictate flame behavior for conditions ranging from free-burning through partial and total extinguishment. In addition, few experiments have been conducted to explore the suppression of well-controlled, turbulent flames. Unlike laminar flames, turbulent flames offer additional features including more intense radiative emissions, structural non-uniformity, and a greater dynamic range of the dominant physical scales. It is postulated that these features affect flame suppression behavior.

The present study seeks to measure the behavioral response of a low-strain, buoyancy-driven, turbulent diffusion flame to a diluted oxidizer stream in a canonical configuration representing the essential features of a suppressed accidental fire. The present facility provides well-controlled inlet conditions, while introducing

* Corresponding author.

E-mail address: awmarsh@umd.edu (A.W. Marshall).

the complicating effects of buoyancy and turbulence characteristic of large-scale fires. The chosen two-dimensional line-flame configuration is especially amenable to a variety of non-intrusive diagnostics. Measurements and observations in this canonical configuration facilitate isolation of suppression effects, while producing suppressed flames with sufficient complexity for applicability to realistic fire scenarios. Of specific interest are variations in flame behavior across a range of suppressed conditions, from extinction-free through partial and total quenching. The present study includes a brief discussion on phenomena characterizing the occurrence of global extinction, though these are not the main focus of the work.

2. Experiment

2.1. Facility

The facility for this study features a Wolfhard–Parker slot burner similar to previous designs [6,7]. The present design is intended to produce a buoyancy-driven, fully-turbulent diffusion flame in a canonical line-fire configuration. The burner is fueled with either methane or propane to yield respective flames with either minimal or appreciable net soot yield. In designing the burner, attributes (burner dimensions and fuel mass flow rate) were purposely selected to ensure the studied flames meet the following geometrical, buoyancy, and turbulence constraints.

The line-fire constraint limits the burner length-to-width aspect ratio so that $L_b/w_b \geq 10$, while also limiting the mean flame height, L_f , so that $L_f/L_b \approx 1$, in order to minimize three-dimensional edge effects. Here, the flame height is approximated via $L_f = \alpha (\dot{Q}_{conv} / L_b)^{2/3}$, where α is a correlation coefficient fitted to preliminary experimental data ($\alpha = 3.0E-4 \text{ m}^{2/3} / \text{W}^{2/3}$) and \dot{Q}_{conv} is the actual convective heat release given by $\dot{Q}_{conv} = \eta_{comb}(1 - \chi_r) \dot{m}_{fuel} \Delta h_{comb}$, where η_{comb} is the combustion efficiency (here assumed to be unity), χ_r is the radiative loss fraction, \dot{m}_{fuel} is the mass burning rate of fuel, and Δh_{comb} is the fuel theoretical mass-based enthalpy of combustion [36].

The buoyancy constraint requires that the flame dimensionless-source-strength (Froude number, \dot{Q}^*) be less than a critical value defining transition between buoyancy-driven and momentum-dominated regimes so that

$$\dot{Q}^* = \frac{\dot{Q}_{conv}/L_b}{\rho_\infty c_{p,\infty} T_\infty \sqrt{g w_b^3}} \leq \dot{Q}_{crit}^* \approx 10 \quad (1)$$

where ρ_∞ , $c_{p,\infty}$, and T_∞ are respectively the density, heat capacity, and temperature of the ambient and g is the gravitational acceleration constant [37].

The turbulence constraint then requires that the flame Grashof number, Gr , evaluated at one-tenth the flame-height, be greater than a critical value defining transition from laminar to fully-turbulent flow according to

$$Gr(z = L_f/10) = \frac{g \beta z^3 (\dot{Q}_{conv}/L_b)}{\rho_\infty c_{p,\infty} \nu_\infty^3} \geq Gr_{crit} \approx 10^{10} \quad (2)$$

where z measures elevation above the fuel port, β is the thermal expansion coefficient of the ambient, and ν_∞ is the ambient kinematic viscosity [38,39].

As guided by the preceding constraints, a slot burner with dimensions of $5 \times 50 \text{ cm}^2$ is selected. For these dimensions, solution of the constraint expressions indicates that methane- and propane-fueled flames with total heat-release rate between roughly 30–55 kW are sufficiently buoyant and turbulent with respect to the original design criteria, and fit the desired line-configuration

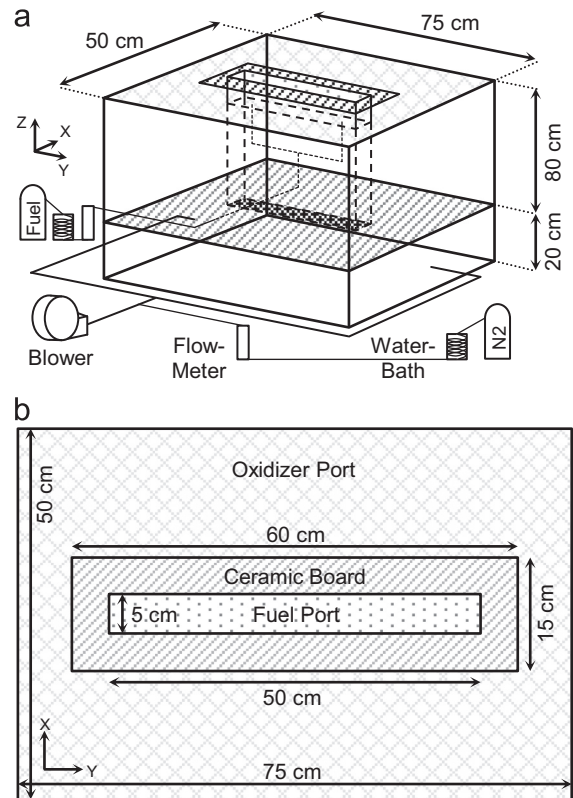


Fig. 1. (a) Diagram of experimental facility. (b) Plan-view of fuel and oxidizer ports.

geometry. Designed from these results, the present burner is illustrated in Fig. 1a and b.

Methane gas (99.5% purity) or propane gas (99.5% purity) is supplied to the burner from respective pressurized cylinders. The fuel initially passes through copper tubing coiled in a water bath, warming it to ambient temperature. The fuel next passes through a needle valve and mass flow meter, before entering the base of the burner through two equally-spaced ports. Fuel enters the burner into a 2 cm tall plenum, then filters through a 5 cm tall bed of fine sand, before discharging through a $5 \times 50 \text{ cm}^2$ stainless-steel slot with 1.5 mm thick walls. For this design, a methane flow rate of $1.00 \pm 0.02 \text{ g/s}$ (nominal 5.4 cm/s from the fuel port) or a propane flow rate of $1.08 \pm 0.02 \text{ g/s}$ (nominal 2.1 cm/s) is utilized. Assuming complete combustion, the total heat-release rate is roughly 50 kW for either fuel in the unsuppressed flames.

Surrounding the burner is an apparatus intended to deliver a uniformly distributed co-flowing oxidizer around the base of the flame. Controlled suppression of the flame is achieved via the introduction of nitrogen gas to the oxidizer stream, providing a full range of suppression conditions from extinction-free through partial and total quenching. The co-flow apparatus was designed with intent to produce a co-flowing oxidizer slow enough to minimally affect the structure of the flame, but robust enough to effectively shield the flame from the ambient room air, ensuring that the flame interacts primarily with the suppressant-laden co-flow environment. The co-flow apparatus and associated flow control systems are also illustrated in Fig. 1a and b.

Air is supplied to the oxidizer stream by an electric centrifugal blower through PVC piping, with flow rate controlled by a manual gate valve and measured with a pitot-static probe and differential-pressure transducer. Sufficient lengths of straight piping are provided upstream and downstream of the probe to ensure fully-developed flow. Airflow measurements are calibrated by adding known amounts of nitrogen to a constant airflow and measuring

the resulting oxygen concentration. A fixed air flow rate of 70 ± 10 g/s (nominal 20 cm/s from the oxidizer port) provides roughly four times the oxygen required for stoichiometric combustion of either specified fuel flow. This maintains a maximum oxidizer velocity an order of magnitude less than a characteristic buoyancy-induced flame/plume velocity, approximated as $u^* = (g L_f \Delta T / T_\infty)^{1/2} \approx 2.9$ m/s, where ΔT is the temperature rise of the plume gases over ambient, here assumed to be roughly 500 K [40].

Nitrogen gas (99.99% purity) for suppression is furnished from a large pressurized Dewar. The nitrogen passes through a 15 m length of copper tubing coiled in a water bath, warming it to ambient temperature to facilitate steady and accurate flow measurement. Nitrogen flow rate is controlled by a needle valve and measured with a rotameter. The nitrogen is injected into the air-flow piping downstream of the airflow metering device, after which the airflow piping is split, with each path delivering half the air/nitrogen mixture to opposite sides of the co-flow apparatus. This supports symmetric delivery of the oxidizer around the burner. Prior to the split, the air/nitrogen mixture passes through a sufficient length of straight piping to ensure well-mixed and fully-developed flow.

The air/nitrogen mixture enters the co-flow apparatus, a sealed rectangular structure with internal dimensions of 50×75 cm². Within the structure, the mixture enters a 20 cm tall plenum mixing space, and passes through a 2 mm thick perforated aluminum plate (40% open area), which serves as a flow-conditioning element. Above the plate is an 80 cm tall upper plenum topped by a 3.2 cm thick aluminum honeycomb with 3.2 mm cells, which ensures a uniform velocity profile at the oxidizer port, as qualitatively verified using flow visualization techniques [41].

On top of the honeycomb and surrounding the fuel port is a thin, 5 cm wide annulus of Kaowool™ ceramic board, positioned so the top of the ceramic board is 20 mm below the lip of the fuel port. This board serves to reduce the oxidizer velocity near the flame base, forcing the onset of buoyancy-generated turbulence upstream toward the fuel port and reducing the tendency to form laminar structures at the base of the flame. This configuration yields entrainment conditions closer to those of a buoyant liquid-pool or solid-fuel fire. Because the entrance flow of the fuel stream is laminar, the flame is expected to be laminar below the transition point to buoyancy generated turbulence, which from Eq. (2), is predicted to occur at roughly $z=2.7$ cm.

Suppression potential is characterized by the oxygen mole-fraction in the oxidizer, X_{O_2} . During experiments, the nitrogen flow rate varies between 0 and 50 g/s, mixing with the fixed air flow to yield variations in X_{O_2} between 0.210 and 0.125.

2.2. Diagnostics

Selected diagnostics involve non-intrusive, integral measurements that capture essential flame features related to strength and behavior through progression to extinction. Measurements include oxidizer-stream X_{O_2} to quantify suppression potential; flame imaging, used for visual identification of flame behavior as well as evaluation of mean flame height; visible flame emissions, which give indirect information about flame sooting behaviors; and infrared flame emissions, which provide flame strength information related to emissive power and radiative loss fraction.

Quantity X_{O_2} is measured using a Servomex 540E paramagnetic oxygen analyzer via a probe located in the oxidizer port. The analyzer provides a measurement accuracy of ± 0.125 mol% O_2 and a response time of 5 s. An additional transport delay averaging around 20 s, is compensated to provide synchronous data collection with other measurements.

Flames are imaged with two digital single-lens reflex cameras. Simultaneous images (± 50 ms) record the front-view (Canon EOS

40D) and the end-view (Nikon D100). An additional video camera (Casio Exilim EX-F1) is used for flame height measurements. Flame images are recorded continuously at 60 Hz using variable exposure settings. Each image is thresholded (via fixed gray value) to a binary black/white image such that white pixels (value 1) correspond to visible flame emissions, while black pixels (value 0) correspond to the absence of flame. Exposure settings are selected to maintain high contrast between the flame and background, minimizing thresholding errors. The set of continuous images is divided into subsets of 600 sequential images (10 s recordings), where this sample size has been found sufficient to produce steady first-order flame shape statistics.

For each subset, the binary images are averaged to obtain a single grayscale image, in which pixel intensity values represent flame intermittency. A contour with a grayscale value of 0.5 then marks locations where a visible flame is present 50% of the time. This contour fits the definition for the 50% intermittent flame height from previous work [42], and is here defined as the mean visible flame shape. The mean height of this contour above the central half of the fuel port (neglecting the end regions) defines the reported L_f measurements. A sample image depicting this technique is provided in Fig. 2.

It should be noted that the presently described image-based L_f measurements rely on visible flame emissions, including the incandescence of soot particles; therefore, measurements reported by this technique include regions of the combustion zone made visible by soot, and do not strictly define the location of the stoichiometric flame sheet. The expanded uncertainty in each L_f measurement is estimated to be less than ± 1.5 cm, from statistical analyses of steady flame measurements.

Visible luminous emissions are measured using a Hamamatsu S2281-01 photodiode and C9051 photosensor amplifier, positioned 190 cm radially outward from the burner centroid, 5 cm above the fuel port, facing perpendicular to the long axis of the burner. This photodiode has a spectral range of 190–1000 nm, a maximum viewing angle of 90° , and a response time of 7 μ s. Neutral density filters (total ND 5.0) shield the sensor to prevent saturation. Background measurements are subtracted to isolate flame emissions.

Using a steady, unsuppressed flame as a light source, the photodiode is calibrated by placing a variety of neutral-density



Fig. 2. Sample image depicting flame height image processing technique. A single flame snapshot (black/white regions) is overlaid with the corresponding mean flame shape (gray contour). $X_{O_2}=0.20$, $L_f=45$ cm.

filters in front of the photosensor and recording the resulting changes in measured signals. Reductions in the signal strength are then correlated to the corresponding net filter transmittance, which defines the ratio of the measured luminosity to that of the unsuppressed flame. The resulting calibration correlation then relates the measured signal of the photodiode to a dimensionless luminosity ratio, LR , normalized to a value of unity for the unsuppressed flame. The expanded uncertainty in each LR measurement is estimated to be less than $\pm 15\%$.

Infrared radiative emissions are measured using a factory-calibrated, water-cooled, MedTherm Schmidt-Boelter type heat-flux transducer, model 64-2-20. The sensor is positioned 100 cm radially outward from the burner centroid, 18 cm above the fuel port, facing perpendicular to the long axis of the burner. This device has a hemispherical absorptance of 0.94 for a spectral range between 0.6–15.0 μm , a maximum viewing angle of 90° , and a response time of 0.25 s. Measurement accuracy is $\pm 3\%$ of responsivity. The convective portion of the measured heat flux is presently neglected and measurements are applied to correct for background irradiation.

Heat flux data are converted to radiative loss fraction, χ_r , using a weighted multipoint radiation source model adapted to the present two-dimensional flame geometry from the original concepts put forth by Hankinson and Lowesmith [43]. This model, while complex, provides a more accurate representation of radiative flame emissions than that given by the simpler and more conventional single-point source model [44]. The single-point source model, which is reasonably accurate when the radiation measurement is recorded sufficiently far from the flame, suffers inaccuracies when the measurement is close enough for source geometrical effects to become important (a fact that will be illustrated later).

Using the multipoint source model, the measured heat flux is assumed to be received from an array of isotropic point sources uniformly distributed over a two-dimensional plane oriented across the visible flame surface. A schematic illustrating this approach is presented in Fig. 3a. The radiative heat flux measured by the transducer, \dot{q}''_g , is determined as the weighted sum of radiation emitted by each individual point source so that

$$\dot{q}''_g = \frac{\chi_r \dot{m}_{fuel} \Delta h_{comb}}{4\pi} \sum_{j=1}^{n_j} \sum_{k=1}^{n_k} w_{j,k} \tau_{j,k} \frac{\cos(\theta_{j,k})}{S_{j,k}^2} \quad (3)$$

where $w_{j,k}$ is a weighting factor applied to the (j,k) th point source, n_j and n_k are respectively the number of point sources in the y and z directions, $\tau_{j,k}$ is the atmospheric transmissivity over the separation distance, $S_{j,k}$, between the (j,k) th point source and the heat flux transducer, and $\theta_{j,k}$ is the angle between the normal out of the transducer surface and the line of sight to the (j,k) th point source. The weighting factors, $w_{j,k}$ must always satisfy $\sum_{j=1}^{n_j} \sum_{k=1}^{n_k} w_{j,k} = 1$.

From Fig. 3a, geometric arguments yield $\cos(\theta_{j,k}) = x_g / S_{j,k}$, and

$$S_{j,k}^2 = x_g^2 + \left[y_g - \left(j - \frac{1}{2} \right) \frac{W}{n_j} \right]^2 + \left[z_g - \left(k - \frac{1}{2} \right) \frac{L}{n_k} \right]^2 \quad (4)$$

where (x_g, y_g, z_g) is the location of the heat flux transducer, and W and L are respectively the width (y) and length (z) of an arbitrary two-dimensional plane containing the flame. For the present study, it is most convenient to define W and L as the boundaries of a recorded flame image. Making the appropriate substitutions and solving Eq. (3) for χ_r then gives

$$\chi_r = \frac{4\pi \dot{q}''_g}{\dot{m}_{fuel} \Delta h_{comb} x_g} \sum_{j=1}^{n_j} \sum_{k=1}^{n_k} \frac{S_{j,k}^3}{w_{j,k} \tau_{j,k}} \quad (5)$$

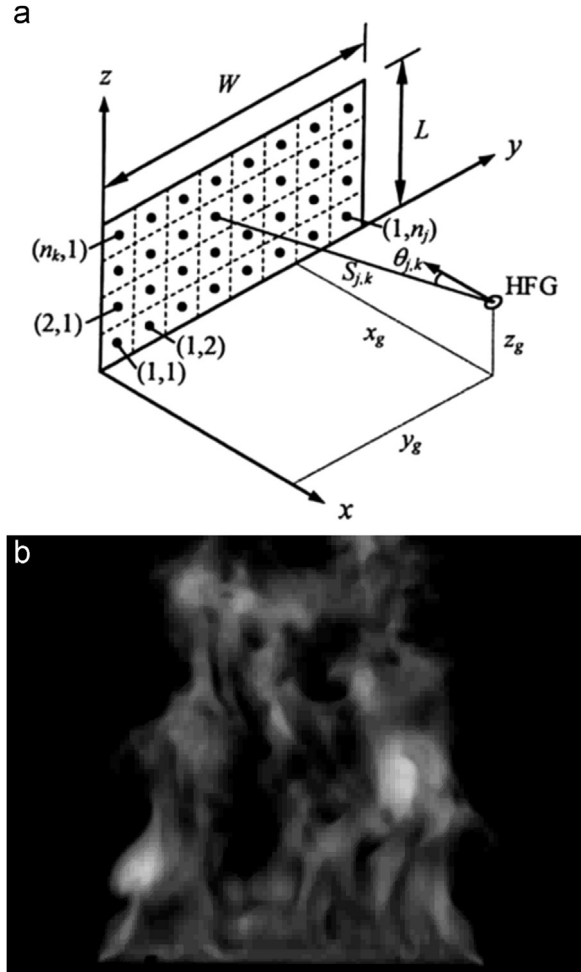


Fig. 3. (a) Diagram depicting multipoint radiation source model. (b) Sample infrared flame image.

Weighing of the point sources is guided using spatially-resolved flame images recorded via a FLIR ThermaCAM[®] SC3000 infrared camera. This device has spectral responsivity between 8 and 9 μm , providing a maximum image resolution of 320×240 pixels at 60 Hz. A sample grayscale infrared flame image is presented in Fig. 3b. Recorded infrared flame images are synchronized with heat flux measurements and averaged over the response time of the transducer. The array of weighting factors applicable to each heat flux measurement is then determined by the corresponding array of pixel intensities, $I_{j,k}$, in the synchronized infrared image so that $w_{j,k} = I_{j,k} / C$, where C is a constant determined by $C = \sum_{j=1}^{n_j} \sum_{k=1}^{n_k} I_{j,k}$.

The array of point sources (n_j, n_k) is bounded by the frame of each infrared image. It is not necessary to assume the flame shape a priori, so long as the entire flame is contained within the frame of the image and background interference is negligible. The flame shape is then resolved within each image, while the peripheral pixels around the flame (for which $I_{j,k}, w_{j,k} = 0$) do not affect the computation. The length-per-pixel is determined by placing an object with known length within the frame of the image, to be referenced during image processing.

For the present study, the flame is resolved as an array of 320×240 individual point sources, representing the full resolution of the recorded images. It is suspected that this level of resolution is not necessary for convergence of the computed radiative loss fraction based on previously reported results [43], which suggest that for axisymmetric flames where point sources can be arranged

one-dimensionally along the flame axis, the multipoint source model is insensitive to the number of point sources when 20 or more are used. A parametric study to evaluate optimal image resolution for the present two-dimensional multipoint source model could also be performed.

The atmospheric transmissivity, $\tau_{j,k}$, in Eq. (5) is presently assumed to be unity for all point sources. This approximation is valid for configurations where the heat flux transducer is relatively close to the flame. For other conditions, such as those incorporating large separation distances and/or an increased presence of water-vapor (such as via water-based suppression), atmospheric transmissivity may be approximated using the methods of Fuss and Hamins [45].

Using Eq. (5) in conjunction with the recorded infrared flame images and weighting factor conventions, χ_r is determined from each heat flux measurement. The expanded uncertainty in each χ_r measurement is estimated to be less than $\pm 4.5\%$.

A comparison between the present multipoint source model and the more conventional single-point source model [44] is illustrated in Fig. 4. For the single-point source model, the radiation source is characterized by a single isotropic point source located at the flame centroid, yielding

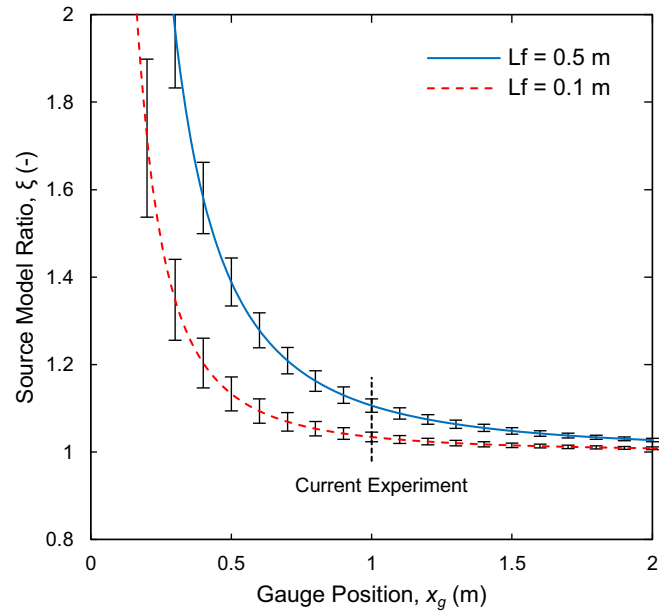


Fig. 4. Ratio of multipoint to single-point radiation source models plotted as a function of gauge position.

$$\chi_r = \frac{4 \pi x_g^2 \dot{q}_g''}{\dot{m}_{fuel} \Delta h_{comb}} \quad (6)$$

analogous to that of Eq. (5).

The ordinate of Fig. 4 plots the ratio of Eq. (5) divided by Eq. (6), which measures the relative agreement between the two source models, while the abscissa plots the gauge position, measured as the perpendicular distance from the flame centroid to the heat flux transducer. The curves in Fig. 4 present source model comparisons for a pair of methane flames with different mean flame heights, roughly 0.5 m and 0.1 m. To produce these curves, source model ratios are computed analytically using thermal images of these flames across a range of gauge positions. No heat flux measurement is required for these calculations.

As shown in Fig. 4, the single-point model underpredicts the multipoint model with decreasing accuracy as the transducer is

moved closer to the flame, an expected result that is consistent with previously reported results for axisymmetric flames [46]. For sufficiently large separation distances where the single-point source model is most valid, the source model ratio correctly asymptotes to unity. Comparing the trends for the two flames, the relative accuracy of the single-point model is shown to vary not only with separation distance, but also with flame geometry, where differences in mean flame height significantly affect the evolution of source model ratio over changing gauge position. Both curves plotted in Fig. 4 follow the functional form $\xi = 1 + \varphi / x_g^2$ (with $R^2 > 0.9995$), where ξ is the plotted source model ratio, and φ is a regression fitting parameter. In general, φ should be characterized solely by the geometry of the radiation source.

For the present study, the heat flux transducer is located at a position where the single-point source model underpredicts the multipoint model by roughly 10%. In order to reduce this discrepancy to less than 1%, the transducer would need to be located at least 2 m away from the flame. Such large separation distances are not always feasible due to space constraints or limitations associated with achieving accurate measurement signal-to-noise ratios. For such situations, the multipoint model presents an attractive alternative.

3. Results and discussion

3.1. Flame images

Figs. 5 (methane) and 6 (propane) present simultaneous front- and end-views of representative flames at selected X_{O_2} . Exposure settings are fixed for these images, which results in extensive saturation at $X_{O_2} = 0.210$ (Figs. 5a and 6a), while providing comparative visibility of the less luminous flames at lower X_{O_2} . All regions of the flames are observed to be sufficiently turbulent, except those immediately above the fuel port. Yellow and blue flame regions respectively indicate soot incandescence and CH luminescence. As X_{O_2} is reduced for both fuels, soot radiation diminishes followed by flame extinction. In Figs. 5 and 6, this is visualized through the transition of flame color from yellow to blue.

In the methane flames, there are minimal observable suppression effects above $X_{O_2} = 0.181$ (Fig. 5b), other than reduction in luminosity. Below $X_{O_2} = 0.180$, the flame base begins to turn blue. Around $X_{O_2} = 0.168$ (Fig. 5c), soot radiation diminishes rapidly, resulting in progressive growth of the blue flame region until roughly $X_{O_2} = 0.163$, at which point the flame appears entirely blue (Fig. 5d). Further reductions in X_{O_2} result in significant flame weakening, evidenced by drastic changes in flame structure and periods of localized detachment from the fuel port, owing to extensive localized quenching. Global extinction is preceded by total detachment of the flame from the fuel port and subsequent liftoff, occurring at $X_{O_2} = 0.151$ (Fig. 5e).

Suppression of the propane flames occur with a largely similar sequence, excepting that notable visual transitions are extended to much lower X_{O_2} . The unsuppressed propane flame is visibly sootier than the methane flame, evidenced by the faint envelope of smoke emanating from the flame sheet (Fig. 6a). Corresponding to this increased sooting propensity, initial bluing of the flame base does not occur until below $X_{O_2} = 0.155$ (Fig. 6b). With further reductions in X_{O_2} , the flame rapidly deteriorates with respect to both soot radiation and overall flame strength, as shown in Fig. 6c ($X_{O_2} = 0.144$), which depicts a partially lifted flame with roughly equal portions of yellow and blue. Transition to an entirely blue flame occurs around $X_{O_2} = 0.140$ (Fig. 6d), with global extinction following shortly thereafter at $X_{O_2} = 0.138$ (Fig. 6e). As with the methane flames, global extinction occurs as detachment and liftoff.

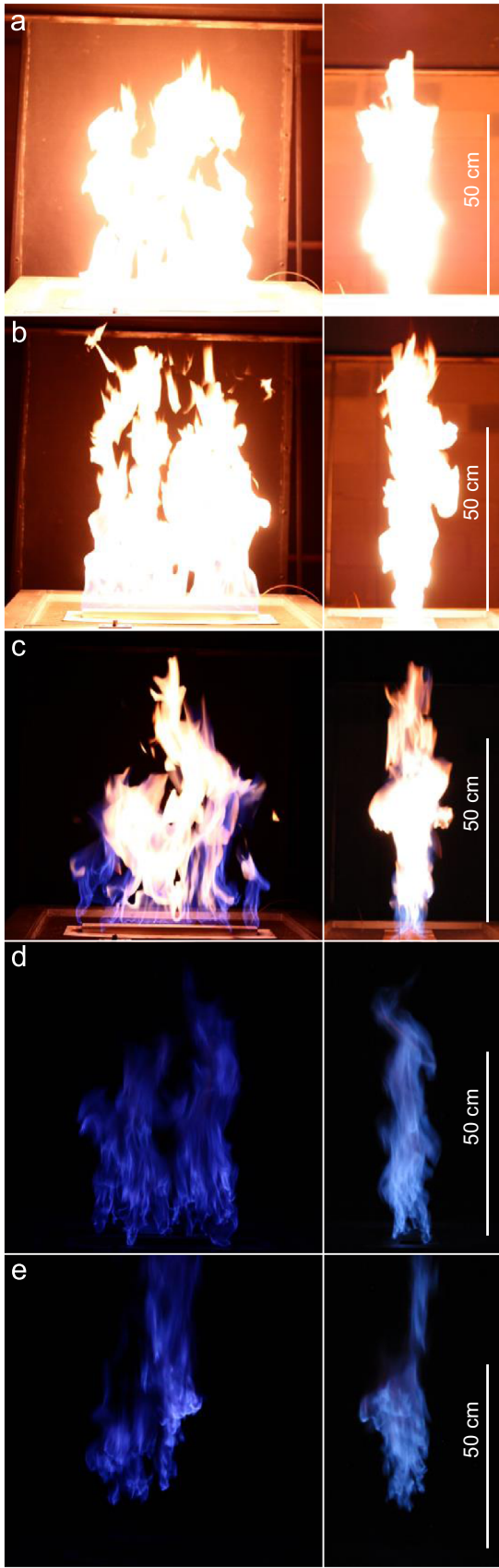


Fig. 5. Simultaneous front- and end-view methane flame images at selected X_{O_2} : (a) 0.210, (b) 0.181, (c) 0.168, (d) 0.158, (e) 0.151. Exposure: 1/30s, f/2.0, ISO 1250. (For interpretation of the references to color in this figure, the reader is referred to the web version of this article.)

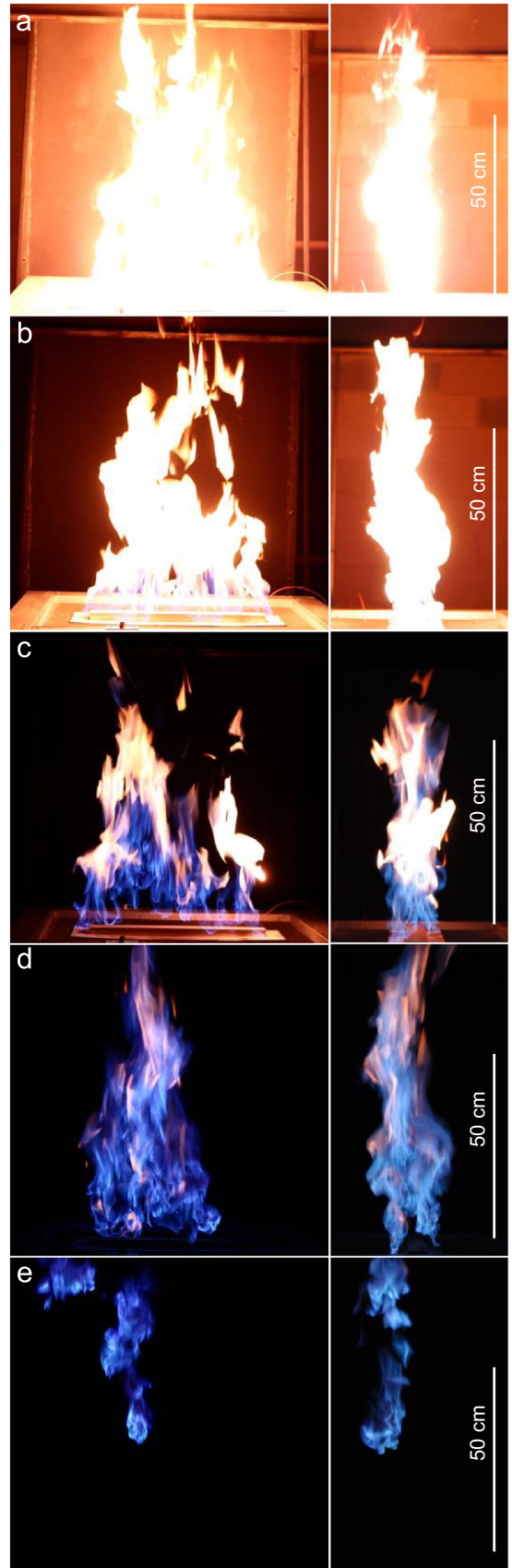


Fig. 6. Simultaneous front- and end-view propane flame images at selected X_{O_2} : (a) 0.210, (b) 0.154, (c) 0.144, (d) 0.140, (e) 0.138. Exposure: 1/30s, f/2.0, ISO 1250. (For interpretation of the references to color in this figure, the reader is referred to the web version of this article.)

Comparing the two fuels, the methane flame experiences complete suppression of soot radiation at a relatively high $X_{O_2}=0.163$, then experiences a prolonged period of stable, soot-free (blue) combustion between $X_{O_2}=0.163$ – 0.153 , prior to extinction. The propane flame, however, does not experience complete suppression of soot radiation until $X_{O_2}=0.140$, in the midst of rampant localized quenching and rapid flame weakening, occurring immediately before extinction at $X_{O_2}=0.138$.

3.2. Flame height

Flame height measurements for both fuels are plotted as functions of X_{O_2} in Fig. 7a. As shown, L_f increases with reducing X_{O_2} , in agreement with previous observations [6,25]. This trend is rationalized that, as X_{O_2} decreases, a greater volume of oxidizer must be entrained to support complete combustion (and soot oxidation). In addition, buoyancy-driven entrainment should decrease due to suppression; therefore the flame must lengthen to entrain the additional required oxidizer, where entrainment rate increases with rising elevation along the flame.

For buoyancy-driven flames, the classical flame height scaling originally developed by Heskestad [47,48] is presented in terms of a dimensionless parameter N , re-derived here for a line-source flame as

$$N = \frac{c_{p,\infty} T_\infty}{g \rho_\infty^2 Y_{O_2}^3 (1 - \chi_r)} \frac{r_{O_2}^3}{\Delta h_{comb}} \frac{(\eta_{comb} \dot{m}'_{fuel})^2}{w^3} \quad (7)$$

where r_{O_2} is the stoichiometric oxygen to fuel mass ratio, \dot{m}'_{fuel} is the fuel mass burning rate per-unit-length of the line-source, w is the width of the flame base, and Y_{O_2} is the oxygen mass fraction of the oxidizer, where Y_{O_2} is simply related to X_{O_2} via $Y_{O_2} = X_{O_2} M_{O_2} / [X_{O_2} M_{O_2} + (1 - X_{O_2}) M_{N_2}]$, and M is the molar mass of the appropriate species. As defined in Eq. (7), N characterizes the environment in which combustion takes place (left term), the properties of the fuel (center term), and the strength/configuration of the fuel source (right term).

Equation (7) is closely related to the original scaling result derived by Heskestad [47], given as

$$\frac{L_f}{D} = f\left(\frac{c_{p,\infty} T_\infty}{g \rho_\infty^2} \frac{r^3}{\alpha \Delta h_{comb}} \frac{\dot{m}'_{fuel}^2}{D^5} \right) \quad (8)$$

In deriving Eq. (7), N is defined as the dimensionless group inside the parentheses in Eq. (8), where the stoichiometric air to fuel mass ratio, r , is expanded as $r = r_{O_2} / Y_{O_2}$ to extend the scaling to oxidizer environments other than ambient air; the convective fraction of the total heat release, α , is re-expressed in terms of the radiative loss fraction as $\alpha = 1 - \chi_r$; and the combustion efficiency, η_{comb} , is included as a coefficient product to the fuel mass loss rate to account for partial suppression of the flame. For line-fire source geometry, as utilized in the present configuration, it follows that an appropriate characteristic dimension of the fuel source, D in Eq. (8), is defined as the width of the flame base, w . It is also convenient to express the fuel mass loss rate, \dot{m}'_{fuel} , as per-unit-length of the fuel port, \dot{m}'_{fuel} . This collection of substitutions yields the result presented in Eq. (7).

The dimensionless parameter N is simply related to the more familiar parameter \dot{Q}^* (Eq. (1)) via

$$N = \left[\frac{c_{p,\infty} T_\infty r_{O_2}}{Y_{O_2} (1 - \chi_r) \Delta h_{comb}} \right]^3 \dot{Q}^{*2} \quad (9)$$

Additional scaling analyses [36,49] suggest that for line-source flames, $L_f / w \propto \dot{Q}^{*2/3}$, but from Eq. (9), $N \propto \dot{Q}^{*2}$, therefore it follows that $L_f / w \propto N^{1/3}$. From the definition for N given by Eq. (7), this

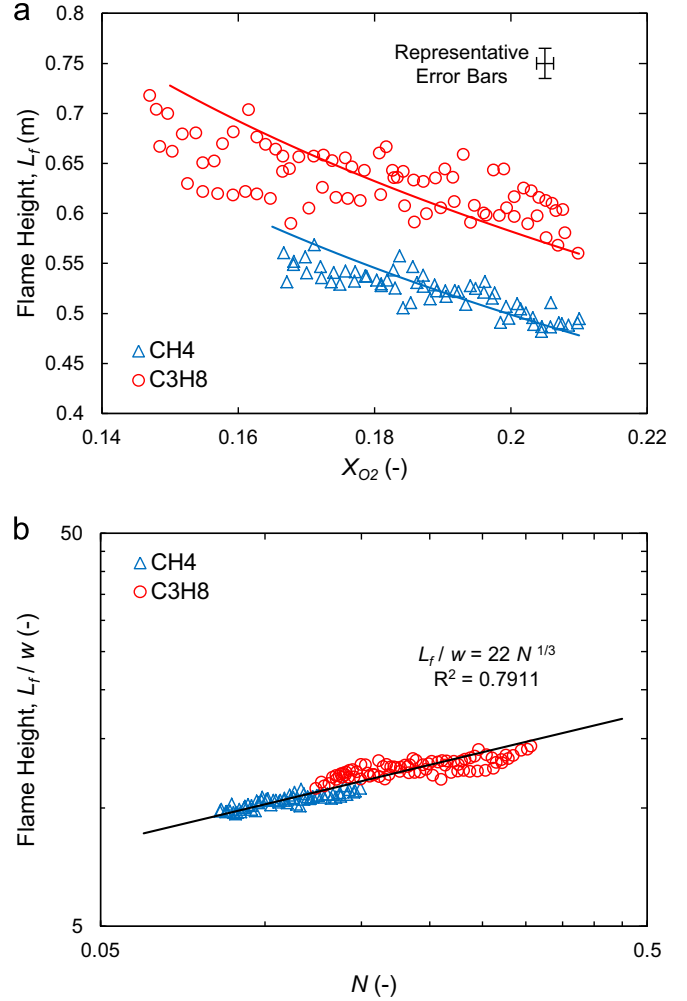


Fig. 7. (a) Measured and predicted L_f for CH₄ and C₃H₈ fuels at varying X_{O_2} . (b) Dimensionless flame height plotted as a function of N .

yields $L_f / w \propto 1/Y_{O_2}$, which reasonably matches the measured trends. Following this scaling relationship, predicted L_f are plotted in Fig. 7a (solid lines) and in Fig. 7b, where predicted and measured L_f are plotted as functions of N . In solving Eq. (7), standard property values for ambient air at 300 K and the specified fuel flow conditions are utilized, while values for χ_r are referenced from the presently measured values given in Section 3.3, and η_{comb} are taken as constant and equal to unity (assuming complete combustion). In Fig. 7a and b, a constant of proportionality of 22 is applied to fit the scaling relationship to the data so that $L_f / w = 22 N^{1/3}$, as plotted in each figure.

As previously introduced, the present method for measuring flame height relies on visible flame emissions which include soot radiation. Soot radiation effects should tend to increase the measured flame height, as the soot burnout region extends beyond the location of the stoichiometric flame sheet. This effect is greatest in the unsuppressed propane flames due to their greater sooting propensity, which helps to explain the higher measured L_f compared to the predicted trend for propane fuel at near-ambient X_{O_2} . The inverse effect, occurring due to soot extinction, explains the slight over-predictions in L_f for methane fuel below $X_{O_2}=0.180$ and propane fuel below $X_{O_2}=0.160$. Similarly declining visible flame height measurements coinciding with flame color transition have been previously reported [25].

Note that no L_f measurements are reported below $X_{O_2}=0.166$ for methane flames, or below $X_{O_2}=0.147$ for propane flames.

Below these respective thresholds, soot radiation in each flame diminishes rapidly, causing an overall reduction in luminosity and transition in flame color from yellow to blue. This transition, along with the development of increasingly transient and intermittent flame structures, result in unsteady flame shape statistics. As a result, L_f data are omitted for these conditions.

3.3. Flame emissions

Raw heat flux and LR measurements for both fuel types are plotted as functions of X_{O_2} in Fig. 8. Here both quantities are plotted on linear axes, making the LR trends difficult to visualize, where values quickly approach zero. These data are alternatively presented in Fig. 9, where now LR measurements are plotted on a logarithmic ordinate and heat flux measurements are re-expressed as calculated χ_r data.

As shown in Fig. 9, LR decreases monotonically with declining X_{O_2} by at least six orders of magnitude for both fuels. From the color flame images discussed in Section 3.1, three flame sooting regimes are identified, each corresponding to transitions in flame color: yellow, yellow-blue, and blue. Notably, the boundaries of these regimes coincide well with the sharp curves in the LR trends. This agreement is noted for both fuels, despite their respective transitions occurring over different ranges of X_{O_2} . Transitions for methane occur at higher X_{O_2} (0.180 ± 0.002 for yellow to yellow-blue, 0.163 ± 0.002 for yellow-blue to blue) than those for propane (0.155 ± 0.002 , 0.140 ± 0.002), owing to the greater sooting propensity of the latter. Despite this, transitions for both fuels occur at roughly equal values of LR , with yellow to yellow-blue transition occurring at roughly $LR = 7E-2 \pm 2E-2$ and yellow-blue to blue transition occurring at roughly $LR = 5E-6 \pm 3E-6$. These trends reinforce the concept that flame luminosity and soot radiation are directly related, as has been previously reported [50].

Unique to the methane LR trend, there is an inflection point within the yellow-blue regime, after which the rapidly declining LR tapers for a prolonged period of quasi-steady, soot-free (blue) combustion between $X_{O_2} = 0.163 - 0.153$. Afterwards, LR shows a steep decline coinciding with flame extinction. In comparison, the propane LR trend experiences continuously sharpening decline

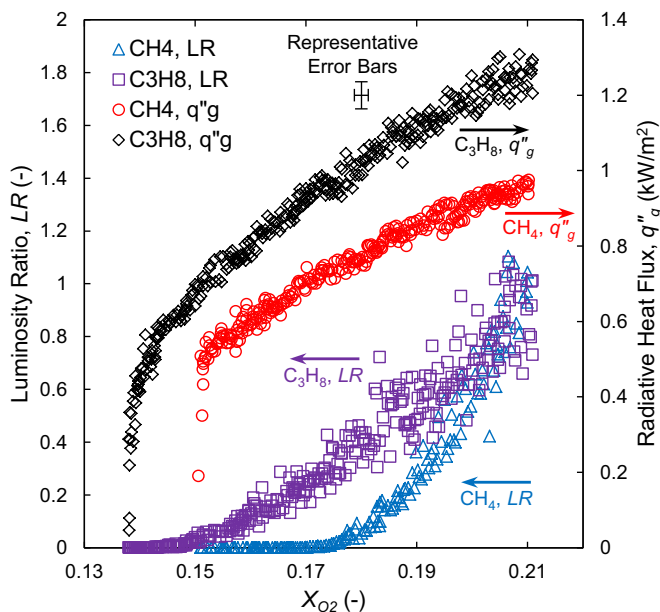


Fig. 8. Linearly plotted raw radiative heat flux and luminosity ratio data for CH_4 and C_3H_8 fuels at varying X_{O_2} .

throughout the yellow-blue and blue regimes. These trends agree well with the preceding flame image observations and suggest that, for the case of methane suppression, soot radiation terminates independently of global flame extinction, whereas for propane suppression, termination of soot radiation and flame extinction happen to occur simultaneously, with the prospect that soot is still present at extinction. This observation is expected to be configuration dependent.

Also plotted in Fig. 9, χ_r measurements decrease linearly for both fuels with declining X_{O_2} . At ambient conditions, χ_r for the propane flame (0.32 ± 0.014) is greater than that for the methane flame (0.23 ± 0.010), values consistent with previously reported measurements [51]. This increase is attributed to greater soot radiation in the propane flame, where broadband soot radiation is detectable in both the visible and infrared spectra. The slope of χ_r decline is then steeper for propane, with flames for both fuels approaching roughly equal χ_r (0.13 ± 0.015) within their respective blue regimes. That the χ_r measurements for both fuels collapse once soot radiation terminates reinforces the notion that their disparity at higher X_{O_2} is principally due to differences in soot radiation. Still, partial quenching effects occurring within the blue regime, particularly for propane, could complicate this interpretation; hence additional analyses should be conducted.

A sharp change in the slope of linear χ_r decline occurs, at $X_{O_2,crit} = 0.152 \pm 0.001$ for methane and $X_{O_2,crit} = 0.142 \pm 0.002$ for propane, in both cases coinciding with the rapid onset of extinction. Based on observations of flame images, the terminal decline of χ_r for both fuels occurs over a period of intermittent flame structural instability, including localized flame lifting at the flame base and expansive localized quenching throughout the flame.

An interesting observation is made when comparing directly the LR and χ_r measurements for the methane flame: measured LR values decrease by four orders of magnitude through the yellow-blue regime, between sharp changes in the surrounding trend, whereas over the same X_{O_2} range, χ_r measures no remarkable change in the otherwise linear decline. This disparity suggests that soot radiation, which is the principal source of the visible emissions, is too weak to significantly impact the infrared emissions, where the latter must then be dominated by the gas-phase spectral emissions of heated combustion products (CO_2 , H_2O) and unburned fuel (CH_4 , C_3H_8). This behavior has been previously reported for laminar flames [24], but not for turbulent flames. Note that this result applies only to the methane flames and is expected to be configuration dependent.

Though the disparity between LR and χ_r trends is clear in the methane flame, it is only loosely present in the propane flame, for which there is observed a slight variation in slope of χ_r decline within the yellow-blue regime. This non-linearity could be attributed to variations in soot radiation, though the effect appears minor, suggesting that contributions from gas-phase emissions in the infrared spectrum remain significant. Causation between changing soot radiation and the observed non-linearity is questionable, however, as it is difficult to disassociate the effects of soot termination and flame extinction that occur simultaneously in the blue regime of the propane flame.

3.4. Flame extinction

The value of X_{O_2} at the point of global extinction is termed the Limiting Oxygen Index (LOI). Published LOI values for suppression of methane and propane flames in nitrogen-diluted air are summarized in Table 1 [28–35]. For the present study, LOI are identified from the recorded flame images as the point when the main flame ceases to exist. The presently measured LOI are listed in Table 1 for (1) standard experimental conditions as previously described (Section 2.1), and (2) conditions identical to (1) but with

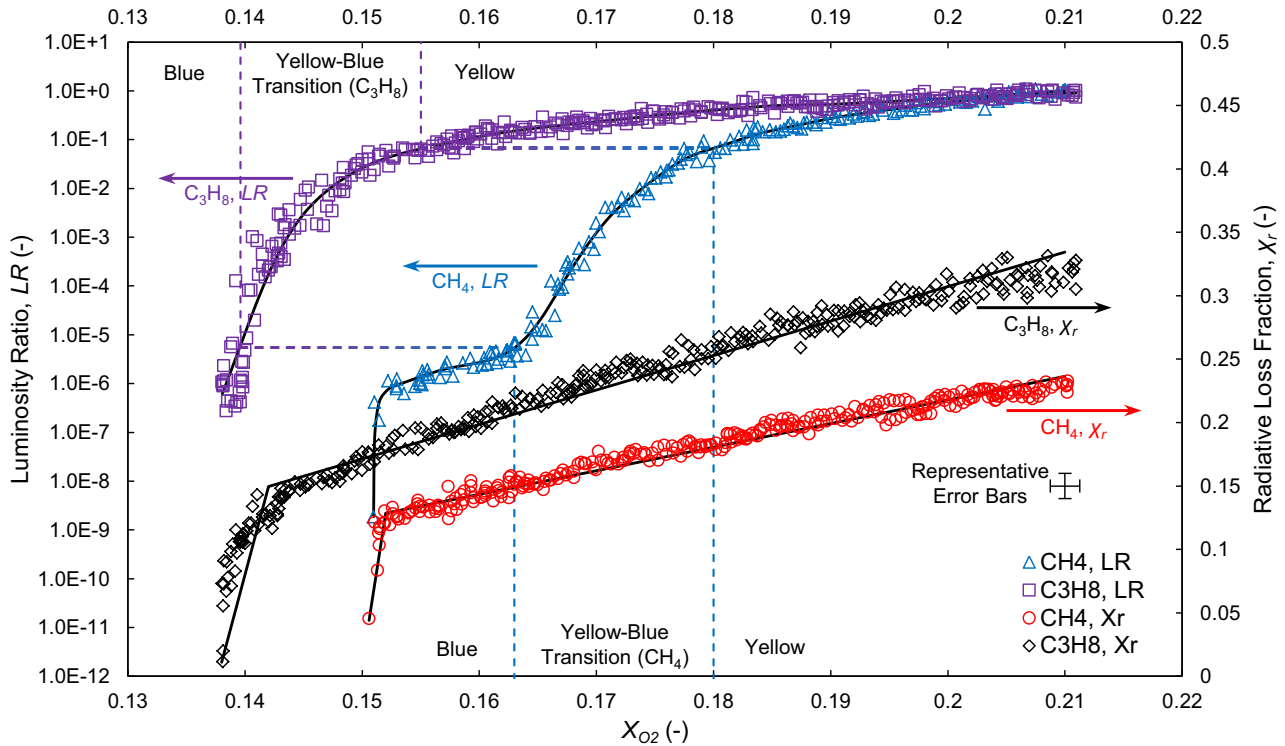


Fig. 9. Luminosity ratio (visible emissions) and radiative loss fraction (infrared emissions) measurements for CH₄ and C₃H₈ fuels at varying X_{O₂}, non-anchored condition (1).

the addition of a flame-base stabilizing ‘oxygen anchor’ (described in detail in Section 3.5).

The *LOI* presented in Table 1 span a range of burner and flow configurations, though only the present study utilizes turbulent flames. Presently measured *LOI* for methane and propane fuels for condition (1) are respectively 0.151 ± 0.002 and 0.139 ± 0.002 . These values are in close agreement with, but slightly lower than, those from other studies using laminar cup-burners. This agreement is attributed to the similarities of both configurations, specifically the observation that global flame quenching occurs immediately following flame detachment and liftoff. That the present study reports slightly lower *LOI* is attributed to the annular ceramic board surrounding the fuel port, which reduces strain and improves stability at the flame base. In fact, measurements in the current configuration without the ceramic board yield $LOI = 0.155 \pm 0.002$ for methane fuel, a result that matches cup-burner values.

From Table 1, it is readily seen that *LOI* are configuration dependent measurements that vary as a function of burner

geometry. Studies using opposed-flow configurations report lower *LOI*, while higher measured *LOI* are reported for the co-flowing configurations, particularly for the Santoro burner. Trends in *LOI* across differing burner geometries are identical for both fuels. The large variations in *LOI* with burner geometry, which are well outside the respective uncertainties noted for each study, are most attributable to variations in flame strain rate and conductive heat losses specific to each type of burner. It is speculated that the lower *LOI* in the opposed-flow configurations are representative of bulk flow quenching, while the higher *LOI* in the co-flowing configurations are in part influenced by flame holding requirements.

Despite the apparent dependence of *LOI* on burner geometry, the presently measured *LOI* are found to be invariant for fuel flow rates between 0.6–1.3 g/s and for oxidizer flow rates between 40 and 70 g/s. Similar results have been previously reported, where the observed extinction limit is believed to be dominated by thermal effects rather than strain related effects [28,32,34,35]. While previous studies have shown that flow conditions can dominate quenching and blowoff behaviors within certain flow

Table 1

LOI values for suppression of methane or propane flames in air diluted with nitrogen.

Source	Burner Type	Flame ^a	Flow ^b	<i>LOI</i> (CH ₄) (mol% O ₂)	<i>LOI</i> (C ₃ H ₈) (mol% O ₂)
Current – Condition (1)	Wolfhard-Parker	T	C	15.1 ± 0.2	13.9 ± 0.2
Current – Condition (2)	Wolfhard-Parker	T	C	13.0 ± 0.2	13.0 ± 0.2
Simmons and Wolfhard [28]	Porous Hemispherical	L	O	13.9 ^c	12.7 ^c
Pitts et al. [34]	Tsuji (Porous Cylindrical)	L	O	14.0 ± 0.1	12.8 ± 0.1
Ishizuka and Tsuji [29]	Tsuji	L	O	14.3 ^c	–
Puri and Seshadri [30]	Opposed-jet	L	O	15.0 ^c	13.7 ^c
Ural [32]	Cup	L	C	15.3 ^c	13.9 ^c
Takahashi et al. [35]	Cup	L	C	15.5 ± 0.2	–
Babb et al. [33]	Cup	L	C	–	14.1 ^c
Hamins et al. [31]	Cup	L	C	–	14.2 ± 0.3
Pitts et al. [34]	Santoro	L	C	16.4 ± 0.1	15.1 ± 0.2

^a Flame regime, Laminar (L) or Turbulent (T).

^b Oxidizer stream flow condition, Co-Flow (C) or Opposed-Flow (O).

^c Uncertainty values not reported.

regimes [26], in the present low-strain, buoyancy-driven flames, these effects are seen to be unimportant in determining the extinction limit.

3.5. Flame liftoff prevention

Initial extinction results for the present study, in agreement with those of previous works [25–27,31–35], show that weakened flames in co-flow lift prior to extinction. As currently understood, this type of extinction is mainly due to weakening of the edge reaction kernel responsible for flame stabilization [25–27], a phenomenon more characteristic of partially-premixed flame suppression, than that of the diffusion flames encountered in fire safety applications. It is then questionable whether/how liftoff extinction relates to the suppression of large-scale turbulent flames, where suppression is believed to result from progressive localized extinction throughout the main combustion region [20–26].

In an attempt to prevent liftoff extinction in the present configuration, an oxygen anchor is applied along the fuel port to strengthen the flame base. Oxygen gas (99.994% purity) is supplied by a pressurized cylinder, with flow rate controlled using a needle valve and measured using an oxygen-calibrated rotameter. The oxygen is delivered via two 60 cm long, 12.7 mm outer-diameter, sintered stainless-steel tubes, each resting on top of the ceramic board, along opposite sides of the burner, adjacent to the edges of the fuel port. The surface of each tube is wrapped with aluminum foil such that oxygen is directed upward at a 45° angle toward the flame base.

The constant oxygen flow rate of $0.080 \pm 8E-4$ g/s (1.2 cm/s from the tube surface) provides less than 2.0% of the oxygen required for stoichiometric combustion of the flame and less than 0.5% of the oxygen supplied by the co-flowing oxidizer stream. Localized X_{O_2} measurements in the vicinity of the oxygen anchor verify that its direct region of influence is limited to within 1 cm from the tube surface. Oxygen anchor effects are thus expected to

negligibly impact the suppression potential of the total co-flowing oxidizer.

Measurements of LR and χ_r for the anchored condition are presented in Fig. 10. All previous discussion points for the previous non-anchored measurements presented in Fig. 9 again apply with the following notable additions. With inclusion of the oxygen anchor, trends in the LR data are shifted toward lower X_{O_2} , where sooting regime transitions for methane occur at $X_{O_2} = 0.178 \pm 0.002$ for yellow to yellow-blue and $X_{O_2} = 0.155 \pm 0.002$ for yellow-blue to blue (0.151 ± 0.002 , 0.131 ± 0.002 for propane). These shifts are attributed to the thermal influence of the oxygen anchor, where locally high X_{O_2} at the flame base spurs increased soot production, resulting in greater soot radiation throughout the flame. Note also that the quasi-steady blue regime preceding extinction of the methane flame is considerably lengthened, occurring between $X_{O_2} = 0.155 - 0.136$. The overall trends in the LR measurements are otherwise similar to those for the non-anchored condition.

As with the non-anchored measurements, χ_r data decrease linearly with declining X_{O_2} . Again, a sharp change in slope occurs, though at lower $X_{O_2,crit}$ for each fuel: 0.143 ± 0.001 for methane and 0.135 ± 0.002 for propane. For $X_{O_2} > 0.152$ for methane and $X_{O_2} > 0.142$ for propane, the oxygen anchor has a negligible effect on χ_r . For X_{O_2} less than these respective limits for each fuel, the oxygen anchor does have an effect, as it prevents lifted flames and their associated extinction.

For the propane flame, the slope of χ_r decline for $X_{O_2} < X_{O_2,crit}$ is similar for both anchored and non-anchored conditions; however, for the methane flame, the slope of χ_r decline for $X_{O_2} < X_{O_2,crit}$ is significantly reduced for the anchored condition. Seemingly, the oxygen anchor is more effective in extending the flammability of the methane flame than that of the propane flame. More interesting however, is that for the anchored condition, the resulting LOI for both methane and propane flames are equivalent (see Table 1). This could suggest that the anchored condition provides a fuel-independent extinction limit that is principally controlled by

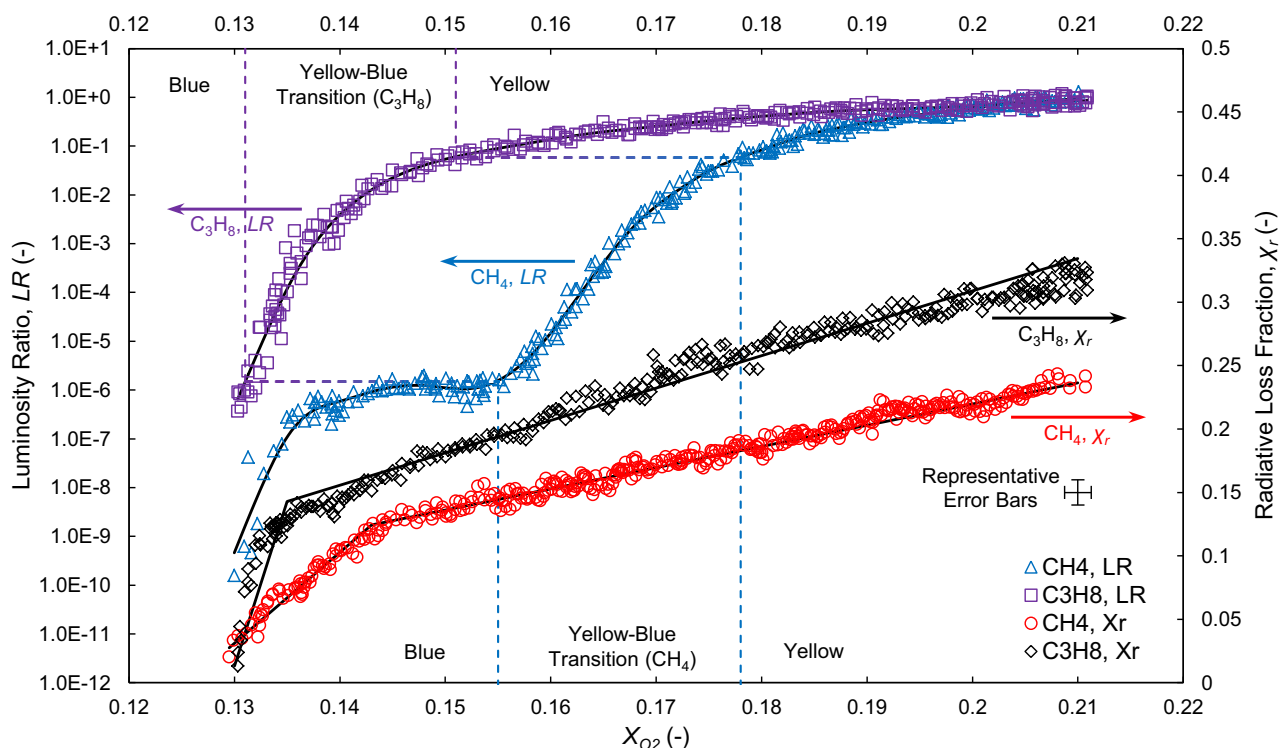


Fig. 10. Luminosity ratio (visible emissions) and radiative loss fraction (infrared emissions) measurements for CH_4 and C_3H_8 fuels at varying X_{O_2} , anchored condition (2).

the oxygen anchor boundary condition, though this would need to be more rigorously shown through additional measurements over a greater variety of fuels.

As shown by the measurements, the oxygen anchor affects not only the extinction condition, but also suppression behavior in advance of the extinction event. While this may or may not be a desirable trait, the oxygen anchor does succeed in its aim of granting a prolonged stable regime, void of flame lifting instabilities, during which measurements can record the behaviors of a substantially weakened flame on the verge of global extinction. This is achieved without the complications of introducing additional fuels for pilot flames or requiring partially premixed inlet conditions. The enhanced flame stabilization provided by this or similar methods could potentially prove useful for future studies of turbulent gas-phase extinction phenomena.

4. Conclusion

Results from a fundamental investigation of flame suppression are presented, featuring buoyancy-driven, fully-turbulent, methane- and propane-fueled diffusion line-flames. For evaluation of infrared flame emissions measurements, a weighted, two-dimensional multipoint source model has been introduced. A scaling analysis for mean flame height (L_f) is also presented, suggesting that for line-source flames, $L_f/w \propto N^{1/3}$, where N is a dimensionless parameter characterizing combustion conditions and w is the width of the flame base. Comparison for both fuels between measured L_f and those predicted by this scaling relationship show very good agreement with a correlation factor of 22.

As the oxygen mole-fraction in the oxidizer (X_{O_2}) is reduced for both fuels, soot radiation diminishes, visualized through a transition of flame color from yellow to blue. Global extinction subsequently occurs, immediately preceded by total detachment and liftoff of the flame from the fuel port. The luminosity ratio (LR), derived from visible emissions measurements, decreases with declining X_{O_2} by at least six orders of magnitude for both fuels, where sharp bends in the trends coincide with transitions in flame sooting behavior between regimes identified by changes in flame color: yellow, yellow-blue, and blue. Transitions for methane occur at higher X_{O_2} (0.180 ± 0.002 ; 0.163 ± 0.002) than those for propane (0.155 ± 0.002 ; 0.140 ± 0.002), owing to the greater sooting propensity of the latter.

Radiative loss fraction (χ_r), derived from infrared emissions measurements, decreases linearly for both fuels with declining X_{O_2} . At ambient X_{O_2} , χ_r is lower for methane (0.23 ± 0.010) than for propane (0.32 ± 0.014), again owing to greater soot radiation in the latter. For non-anchored flames, a sharp change in the slope of linear χ_r decline occurs, at $X_{O_2,crit} = 0.152 \pm 0.001$ for methane and $X_{O_2,crit} = 0.142 \pm 0.002$ for propane, in both cases coinciding with the rapid onset of extinction. For the methane flame, χ_r data appear to be non-responsive to sharp changes in the LR trend, suggesting that soot radiation is important in the visible emissions, but too weak to significantly impact the infrared emissions.

Presently measured values of the Limiting Oxygen Index (LOI) for suppression of methane and propane flames via nitrogen diluted air are respectively 0.151 ± 0.002 and 0.139 ± 0.002 . These values are in close agreement with, but slightly lower than, those from other studies using laminar cup-burners. Further, LOI are seen to be configuration dependent measurements, varying significantly with burner geometry. To explore extinction without liftoff, an 'oxygen anchor' has also been applied along the fuel port to stabilize the flame base. With the oxygen anchor, lifted flames

are prevented, extending the domain of flammability for both fuels to roughly equivalent LOI of 0.130 ± 0.002 .

Acknowledgments

This project is supported by the U.S. National Science Foundation (NSF-GOALI Award #1236788). Discussions with S. Vilfayeu, T. Myers, N. Ren, and Y. Wang are gratefully acknowledged. Special thanks go to Prof. C. Cadou for loaning the infrared camera used in this study.

References

- [1] J.R. Mawhinney, B.Z. Dlugogorski, A.K. Kim, *Fire Saf. Sci. Proc. Int. Symp.* 4 (1994) 47–60.
- [2] B. Downie, C. Polymeropoulos, G. Gogos, *Fire Saf. J.* 24 (1995) 359–381.
- [3] B. Yao, W. Fan, G. Liao, *Fire Saf. J.* 33 (1999) 129–139.
- [4] A. Atreya, T. Crompton, J. Suh, *Fire Saf. Sci. Proc. Int. Symp.* 6 (2000) 493–504.
- [5] G. Grant, J. Brenton, D. Drysdale, *Prog. Energy Combust. Sci.* 26 (2000) 79–130.
- [6] C.C. Ndubizu, R. Ananth, P.A. Tatem, V. Motevalli, *Fire Saf. J.* 31 (1998) 253–276.
- [7] K. Prasad, C. Li, K. Kailasanath, C. Ndubizu, R. Ananth, P.A. Tatem, *Combust. Sci. Tech.* 132 (1998) 325–364.
- [8] A.M. Lentati, H.K. Chelliah, *Symp. Int. Combust.* 27 (1998) 2839–2846.
- [9] K. Prasad, C. Li, K. Kailasanath, *Fire Saf. J.* 33 (1999) 185–212.
- [10] A.K. Lazzarini, R.H. Krauss, H.K. Chelliah, G.T. Linteris, *Proc. Combust. Inst.* 28 (2000) 2939–2945.
- [11] G.O. Thomas, *Combust. Flame* 130 (2002) 147–160.
- [12] B.T. Fisher, A.R. Awtry, R.S. Sheinson, J.W. Fleming, *Proc. Combust. Inst.* 31 (2007) 2731–2739.
- [13] R. Ananth, R.C. Mowrey, *Combust. Sci. Tech.* 180 (2008) 1659–1692.
- [14] I. Sakurai, J. Suzuki, Y. Kotani, H. Naito, A. Yoshida, *Proc. Combust. Inst.* 34 (2013) 2727–2734.
- [15] A. Jenf, A. Collin, P. Boulet, G. Pianet, A. Breton, A. Muller, *Fire Saf. J.* 67 (2014) 1–12.
- [16] Y. Xin, K. Meredith, *Fire Saf. Sci. Proc. Int. Symp.* 11 (2014).
- [17] Y. Wang, K. Meredith, X. Zhou, P. Chatterjee, Y. Xin, M. Chaos, N. Ren, S. Dorofeev, *Fire Safety Sci. Proc. Int. Symp.* 11 (2014).
- [18] T.M. Jayaweera, H.-Z. Yu, *Fire Saf. J.* 43 (2008) 63–70.
- [19] H.-Z. Yu, *Fire Saf. Sci. Proc. Int. Symp.* 11 (2014).
- [20] B.H. Chao, C.K. Law, J.S. T'ien, *Sym. Int. Combust.* 23 (1990) 523–531.
- [21] J.L. Rhatigan, H. Bedir, J.S. T'ien, *Combust. Flame* 112 (1998) 231–241.
- [22] K. Santa, B.H. Chao, P.B. Sunderland, D.L. Urban, D.P. Stocker, R.L. Axelbaum, *Combust. Flame* 151 (2007) 665–675.
- [23] V.R. Lecoustre, P. Narayanan, H.R. Baum, A. Trouvé, *Fire Saf. Sci. Proc. Int. Symp.* 10 (2011) 583–596.
- [24] P. Narayanan, H.R. Baum, A. Trouvé, *Proc. Combust. Inst.* 33 (2011) 2539–2546.
- [25] J. Min, F. Baillet, H. Guo, E. Domingues, M. Talbaut, B. Patte-Rouland, *Proc. Combust. Inst.* 33 (2011) 1071–1078.
- [26] J. Min, F. Baillet, *Combust. Flame* 159 (2012) 3502–3517.
- [27] F. Takahashi, V.R. Katta, G.T. Linteris, O.C. Meier, *Proc. Combust. Inst.* 34 (2013) 2707–2717.
- [28] R.F. Simmons, H. Wolfhard, *Combust. Flame* 1 (1957) 155–161.
- [29] S. Ishizuka, H. Tsuji, *Sym. Int. Combust.* 18 (1981) 695–703.
- [30] I.K. Puri, K. Seshadri, *Combust. Flame* 65 (1986) 137–150.
- [31] A. Hamins, G. Gmurczyk, W. Grosshandler, R.G. Rehwoldt, I. Vazquez, T. Cleary, NIST SP861 (1994) 345–465.
- [32] E.A. Ural, *Proc. Halon Options Tech. Working Conf.* 9 (1999) 275–283.
- [33] M. Babb, S.R. Gollahalli, C.M. Sliepcevich, *J. Prop. Power* 15 (1999) 260–265.
- [34] W.M. Pitts, R. Bryant, J. Yang, *Proc. Joint Meet. U.S. Sect. Combust. Inst.* 2 (2001) 1–16.
- [35] F. Takahashi, G.T. Linteris, V.R. Katta, *Proc. Combust. Inst.* 31 (2007) 2721–2729.
- [36] Y. Hasemi, M. Nishihata, *Fire Saf. Sci. Proc. Int. Symp.* 2 (1989) 275–284.
- [37] M.A. Delichatsios, *Combust. Flame* 92 (1993) 349–364.
- [38] S. Kimura, A. Bejan, *Int. J. Heat Mass Trans.* 26 (1983) 1515–1532.
- [39] K. Noto, K. Teramoto, T. Nakajima, *J. Thermophys. Heat Trans.* 13 (1999) 82–90.
- [40] G. Heskestad, *Combust. Flame* 118 (1999) 51–60.
- [41] L.I. Gaby, *J. Sci. Instrum.* 43 (1966) 334.
- [42] E.E. Zukoski, B.M. Cetegen, T. Kubota, *Symp. Int. Combust.* 20 (1984) 361–366.
- [43] G. Hankinson, B.J. Lowesmith, *Combust. Flame* 159 (2012) 1165–1177.
- [44] A.T. Modak, *Combust. Flame* 29 (1977) 177–192.
- [45] S.P. Fuss, A. Hamins, *Fire Saf. J.* 37 (2002) 181–190.
- [46] Y.R. Sivathanu, J.P. Gore, *Combust. Flame* 94 (1993) 265–270.
- [47] G. Heskestad, *Symp. Int. Combust.* 18 (1981) 951–960.
- [48] G. Heskestad, *Fire Saf. J.* 5 (1983) 103–108.
- [49] B.S. Grove, J.G. Quintiere, *J. Fire Prot. Eng.* 12 (2002) 117–137.
- [50] A.J. Giovanetti, D.P. Hoult, J.C. Keck, A.F. Sarofim, U.S. D.O.E. Report MIT 2298-80-1, 1980.
- [51] A. Hamins, K. Konishi, P. Borthwick, T. Kashiwagi, *Symp. Int. Combust.* 26 (1996) 1429–1436.